Optimization of trajectory processing algorithms to print 3D circuit boards using piezo ink jet and 6-axis robots

Davide Beneventi, Andrea Graziano, Gioia Furia, Lionel Charpin, Mathieu Jean-Louis

Optimization of trajectory processing algorithms to print 3D circuit boards using piezo ink jet and 6-axis robots

Davide Beneventi,[a,*] *Andrea Graziano*,[a] *Gioia Furia*,[a,+] *Lionel Charpin*,[b] *Mathieu Jean-Louis*[c]

[a] Univ. Grenoble Alpes, CNRS, Grenoble INP,[¥] LGP2, F-38000 Grenoble, France

[¥] Institute of Engineering Univ. Grenoble Alpes

[b] AlpRobotic, 88 rue de Chartreuse, 38420 Le Versoud, France

[c] Rtone, 4 rue Maurice Moissonnier, 69120 Vaulx-en-Velin, France

[+] Now with CEA Grenoble, France.

E-mails:

Davide Beneventi *corresponding author: davide.beneventi@pagora.grenoble-inp.fr

Andrea Graziano: arch.a.graziano@gmail.com

Gioia Furia: gioia.furia@cea.fr

Lionel Charpin: charpin@alprobotic.fr

Mathieu Jean-Louis: mathieu.jean-louis@rtone.fr

Abstract

Direct printing of conductive inks at the surface of generic 3D objects using 6 axis robots is attracting an ever-increasing interest, however the high precision positioning and the generation of smooth printing trajectories still represent a bottleneck for the manufacturing of 3D electronic circuits. This work presents a new approach for the rapid prototyping of 3D electronics onto generic objects using a 6 axis robot equipped with a piezo jetting printhead and a high speed laser profiler and a six steps protocol composed by the: i) 3D scan of the substrate and mesh smoothing, ii) 2D circuit projection on the planarized mesh and generation of the 3D trajectory, iii) normals alignment of points lying in the 3D trajectory, iv) retrieve of the effective toolhead TCP translation speed along the 3D trajectory with a blank run, v) synchronization of the ink jetting frequency with the effective toolhead speed, vi) generation of the robot code and print.

The effect of mesh and normals smoothing and of circuit design on the effective toolhead translation speed was systematically investigated in order to minimize speed

fluctuations/heterogeneous ink deposition during printing, the computational load and shape deviation from the pristine 3D substrate.

Conductive tracks printed on an ABS dome displayed geometry and line resistance in line with those predicted by a semi-empirical model using the robot nominal speed and silver ink conductivity, thus showing that the robot operated under stable and well controlled conditions during the printing process.

The developed process displayed an average duty cycle of ca. 30 min from the 3D scan to the printing of the 3D circuit, thus showing that it could be suitable for the rapid prototyping/benchmarking of 3D electronics on generic objects.

Keywords

Six-axis robot, Jetting, Printed electronics, Lines morphology, Conductivity.

1. Introduction

Over the last decade, additive manufacturing (AM) progressively evolved from a laboratory curiosity to a ubiquitous manufacturing approach able to process a wide variety of materials (i.e. from metal powders to cell-inoculated hydrogels) for the production of both structural and functional objects [1]. Moreover, the straightforward link between the digital model and the final physical product allows including additive manufacturing among the production processes driving the Industry 4.0 revolution [2]. Despite the wide variety of technologies implemented on 3D printers, most of commercial processes are based on the use of cartesian robots and on the layer by layer construction of the 3D object. The intrinsic limitations of this approach, such as the generation of anisotropic objects and the impossibility to deposit material along out-of-plane freeform paths [3], led to an ever-increasing interest for poly articulated industrial robots. Owing to i) their ability to follow freeform trajectories while keeping a controlled orientation of the dispensing tool, ii) the ease of scale-up, and iii) high payload/positioning and repeatability, 6-axis arms have been recently identified as ideal manipulators to carry dispensing tools and have been integrated in both conventional AM technologies [3]-[5] and hybrid additive-subtractive processes [6].

Recent studies on cold spray [7] and hydrogel [8] deposition on non-planar substrates highlighted that the redundant degree of freedom of 6 axis robots imposes to tightly correlate the material dispensing tool characteristics, the geometry of the printing substrate and the tool head velocity in order to depose high-precision patterns. In order to develop a general method

for the generation of freeform printing trajectories, algorithms to optimize the generation of printing paths accounting for robot joints kinematics [9] and to fit 2D trajectories on regular 3D substrates [10] with minimum deformation have been recently proposed demonstrating that, despite the inherent complexity of 6 axis manipulators, a simplified approach can be envisaged. As observed earlier for structural and large-scale applications [4], the use of poly articulated manipulators is triggering an ever-increasing interest for the AM of 3D electronics.

Leaving aside the manipulator technology, most of additive manufacturing processes have been developed to process one-two materials with the aim of manufacturing structural objects. Only after the pioneering works of Macdonald [11] and Lewis [12], where conventional FDM 3D printing was coupled to needle-dispensing of conductive inks in order to embed conductive paths into 3D plastic objects, a wide variety of multi materials AM processes have been developed [13]-[15] allowing the simultaneous fabrication of both structural and electronic components. Electronic circuits surface integration has been also proposed as alternative to their bulk integration into 3D objects and high line density circuits on complex 3D shapes have been manufactured by lased direct structuring (LDS) of conductive paths on injection-moulded plastics [16]-[19]. Regardless of the high precision and high conductivity of surface circuits obtained by LDS, this manufacturing technology relies on the use of a specific thermoplastic composite and a sequence of laser etching and metallization steps [16] which preclude its use to generic 3D objects. The direct printing of conductive and dielectric inks by piezo jetting [20], ink jet and aerosol spray [21] or needle dispensing [22] appear as a viable alternative to LDS. Indeed, recent studies demonstrated that the integration of piezo or pneumatic jetting printheads on a 6-axis robot can be effectively used to print silver tracks on a 3D paper substrate [23], RF antennas on PC-ABS objects [24],[25] and large-scale composites [26]. Whereas, pneumatic needle dispensing has been used to print conductive tracks during the 3D printing of a PLA helicoidal structure on a double robot bench [27].

Despite first works demonstrate that 6 axis robots can be effectively used to print electronic circuits on the surface of generic 3D objects, the control of the full process (i.e. from the definition of the 3D object, circuit design and the identification/optimization of trajectory processing algorithms to high precision circuit board printing) and its impact on the final print quality remains rather unexplored. The aim of this work is to investigate a 3D circuits printing process based on the 3D scan of a generic object followed by the transfer of 2D circuits on the object surface and the generation of smooth 3D printing trajectories using the combination of mesh-and normals-smoothing algorithms. In order to validate the viability of the proposed process, the trajectory generation and printing conditions optimized on model geometries (semi

spherical substrate and simple circuit design) were used to design and print a hybrid 3D circuit board including surface mount discrete components, a USB PCB and a NFC antenna.

2. Materials and methods

2.1 Printing cell

Cell setup. A inhouse designed robotic cell [23], composed of a 6-axis robot (Staubli TX2 60, 670 mm range and 0.02 mm repeatability) equipped with a high-speed laser profilometer (Keyence, LJ-V7080/LJ-X8000A) and a piezo jetting dispensing valve (Vermes MDV 3200A) mounting a 0.1 mm nozzle was wired and mounted on a low vibration bench (AlpRobotic, France). The laser profilometer was used to scan the surface of 3D objects at speeds of 40 or 50 mm/s and sampling frequencies of 200 and 1000 Hz, corresponding to sampling periods of 200 and 50 µm, respectively. The planar scan trajectory was made of 10 cm length parallel lines with a step of 3 cm. Height data were retrieved as .csv files and combined. The scan tool centre position (TCP) was used to obtain the coordinates of each sampled point in the robot reference cartesian system (World). Sampling periods (d) of 0.2 and 0.05 mm were used to obtain low or high definition 3D scans which were processed in order to generate the printing trajectory and to analyse the morphology of printed paths, respectively.

The piezo jetting non-contact technology was selected for this study since: i) it allows processing high density inks with limited/no flowing when deposed on inclined/vertical surfaces, ii) the printhead can be operated at a distance of 1-3 mm from the substrate thus preventing the collision of the printhead with the substrate in case of inaccurate calibration of the robot-printhead kinematic chain. The jetting valve has a fully programmable duty cyle. In this study the tappet-rising, -opening and -falling time had constant values (of 0.5, 2 and 0.2 ms, respectively), whereas, the delay time between each dispensing cycle was varied between 0.1 and 1000 ms in order to adapt the overall jetting frequency to the printing speed (i.e. the jetting valve TCP speed) and the desired path width using a semi-empirical model developed in a previous study [23].

a)  b) 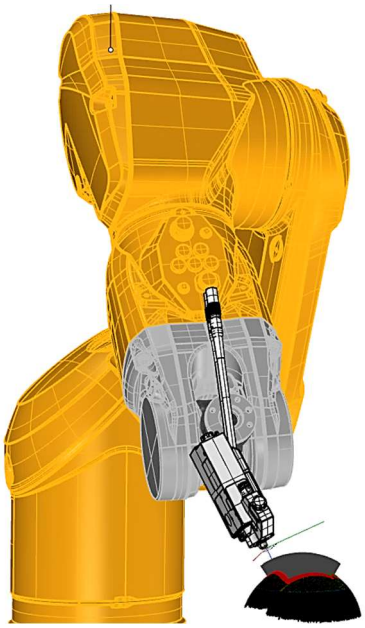

Fig. 1. Detail of the robotic cell developed in this study and 3D printed ABS half sphere used as model substrate a). Screenshot of the offline programming environment b).

Offline programming. The offline programming protocol was developed using a commercial CAD software, Rhinoceros 3D (Robert McNeel & Associates, USA), and two additional plugins, i.e. Grasshopper and RhinoRobot (Kinematiq, France).

The protocol to generate an accurate and smooth printhead trajectory and to synchronize the ink jetting frequency with the printing speed was based on four sequential operations:

i) Meshing and smoothing points obtained with the laser profilometer. In order to remove the measurement noise, points were meshed using rectangular cells and the Paul Bourke (PB) smoothing method [28], i.e.:

$$P_i' = P_i + \frac{1}{n}\sum_{j=0}^{n-1}\left(P_j - P_i\right) \quad (1)$$

where, P_i' is the smoothed point, n is the number of points P_j surrounding the pristine point P_i (i.e. $n = 4$ for rectangular cells). Two major constrains dictated the number of loops when applying the PB smoothing method:

- the offset of smoothed points with respect to the pristine ones, had to be < 200 µm in order to limit the scattering of the smoothed mesh from the real geometry.
- the computational load, ie. the number of basic operations necessary to obtain a sufficient noise reduction both in terms of point position and orientation of normals to the 3D mesh, which for the PB method is $Nbo_{PB} = 30\ \left[\frac{operations}{point\ x\ loop}\right]$.

ii) Transferring 2D paths on the 3D mesh with minimum geometric deformation. Planar circuits were transferred on 3D substrates, using quasiisothermic mesh parametrization [29] and planarization (GrassHopper, Kangaroo). 2D circuit curves are discretized with 0.2 mm resolution, positioned, and then projected on the planarized mesh in order to extract their points' positions in terms of mesh face number and mesh parameter (position on the mesh face). Curves are then reconstructed as polylines onto the original 3D mesh using the mesh face number and points parameters. Length variations between 2D and 3D homologue curves are then calculated to evaluate the deformation induced by the transformation.

iii) Smoothing normals to the 3D mesh of points in the 3D circuit in order to remove the noise generated by the discrete mesh. The normal orientation alignment algorithm (NA) aims at smoothing the robotic toolpath in terms of cinematic rotations, allowing a more homogeneous traveling speed. The iterative algorithm for each trajectory point *i* checks the adjacent vectors and does the average, ϑ_i', of the three (the previous one θ_{i-1}, the considered one θ_i, and the next one θ_{i+1}):

$$\vartheta_i' = \frac{\theta_{i-1}+\theta_i+\theta_{i+1}}{3} \quad (2).$$

In this way, the direction of each vector tends to align to the contiguous vectors reducing normals oscillations due to the scan mesh geometry and noise. As for mesh smoothing, the angular scattering among normals of neighbouring points and the computational load, which for the NA is $Nbo_{NA} = 9\ \left[\frac{operations}{point\ x\ loop}\right]$, where used to constrain the number of loops.

iv) To synchronize the jetting frequency with the effective printhead speed/position along the trajectory. Since the complex kinematic and the presence of singularities does not allow poly articulated robots to keep a constant speed along 3D paths, the TCP speed was retrieved during a blank run along the printing trajectory. According to a semi-empirical model described in a previous work [23], the average speed (V_T), the diameter of individual ink drops ejected by the printhead (ϕ_0 = 0.280 mm in the tested conditions) and the target line width (w) were used to calculate the jetting frequency (F_J) and the drop number (n_d) necessary to print the path using the equations:

$$w = \frac{S\phi_0}{2} \cdot \left\{ \frac{\pi}{2\cdot(1-C)} - \left[\frac{Sin^{-1}\sqrt{1-(1-C)^2}}{1-C} - \sqrt{1-(1-C)^2} \right] \right\} \quad (3)$$

and

$$n_d = L\frac{F_J}{V_T} \quad (4),$$

where

$$C = \frac{\phi - \frac{V_T}{F_J}}{\phi} \quad (5)$$

is the linear coverage ratio between adjacent drops, L is the length of the printed line and $S = \frac{1.5}{1-0.58 \cdot C^{4.7}}$ is the experimental drop spreading coefficient for the tested Ag ink as determined measuring the diameter of 2-10 superimposed drops printed on the ABS substrate (Fig. 2.).

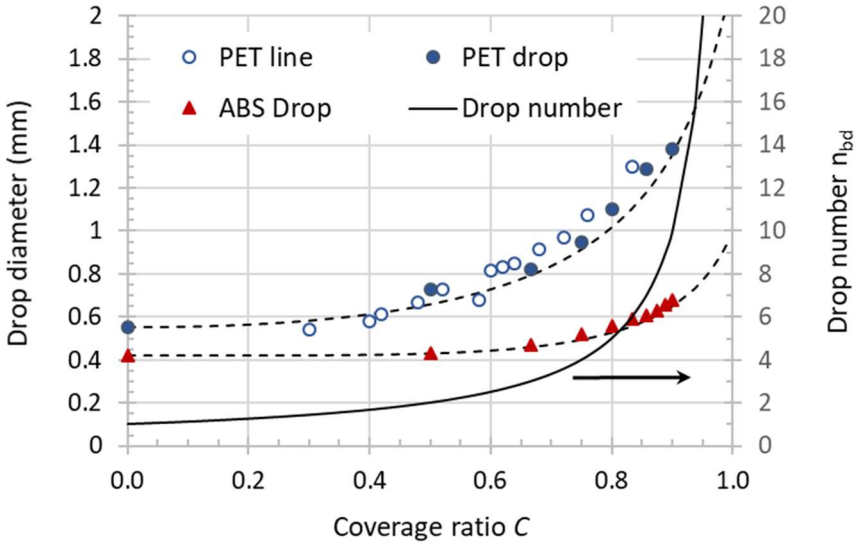

Fig. 2. Influence of the coverage ratio and of the number of superimposed unit drops, $n_{bd} = \frac{1}{1-C}$, on the diameter of the printed dot. Data obtained on a smooth PET film were added to compare ABS with a substrate with good ink spreading.

2.2 Printing of conductive inks.

Effect of smoothing and circuit design on the printing speed. The effect of circuit design and smoothing on the printing speed was quantified using an ABS 3D printed semi sphere (45 mm-radius, 0.1 mm layer) polished with a P600 sandpaper and the two planar circuits shown in Fig. 3.a and b. Right angles in the circuits were filleted with radii ranging between 0 and 4 mm and they were printed with a jetting frequency of 89 Hz corresponding to a drop coverage ratio of 66%. The circuit shown in Fig. 3.c was used to evaluate the print accuracy with a reduced pitch and to limit the line width it was printed using a jetting frequency lowered to 75 Hz (i.e. a drop coverage ratio of 60%).

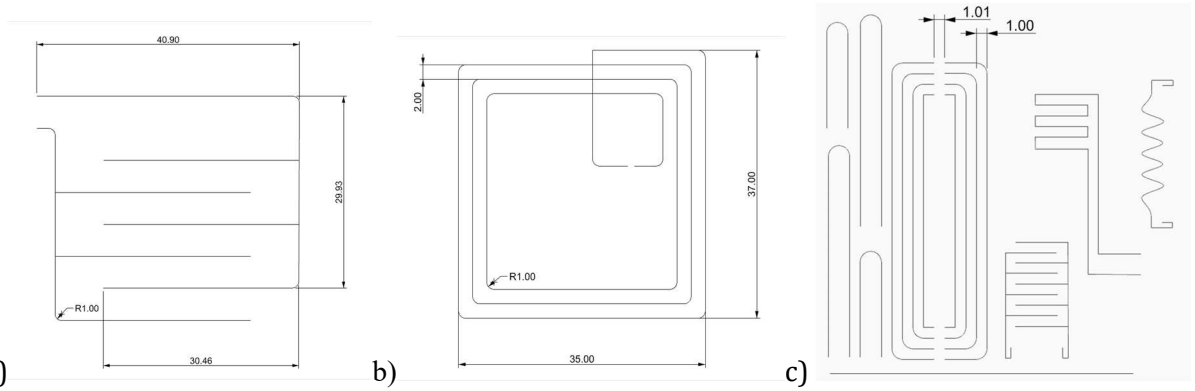

a) b) c)

Fig. 3. Planar circuits design used in this study. a) Large interdigitated path, b) antenna-type three-windings coil, c) patterns with 1 mm pitch.

Owing to the absence of tiny details on the 3D substrate and to limit the number of points to process, the 3D scan sampling period (d) of 0.2 mm was under sampled to 0.4 mm and the region of interest was restricted to the print area, i.e. a spherical dome with a base diameter of 50 mm. Fig. 4.a shows that he planar scan with a fixed sampling period d generates rectangular cells with size (l_i) and normal angle deviation between neighbouring cells (ϑ_i) depending on the point distance from the centre of the half-sphere:

$$l_i = R\left[Cos^{-1}\left(\frac{R-D_i-d}{R}\right) - Cos^{-1}\left(\frac{R-D_i}{R}\right)\right] \tag{6}$$

$$\vartheta_i = \frac{l_i}{R}\frac{180}{\pi} \tag{7}$$

where $D_i = i\,d$ is the distance from the half sphere centre and i the number of considered periods.

According to eq. (6) and (7) the minimum angle variation with a sampling step of 0.4 mm is 0.51 deg (Fig. 4.b) and, in the region of interest, it has an average value of 0.53 deg which was considered as the target value in order to obtain a noise-free trajectory after PB smoothing.

According to the lower computational load of the normal smoothing algorithm NA, 3D circuits were discretized with a period of 0.2 mm, corresponding to a target angle variation of 0.25 deg for a noise-free trajectory.

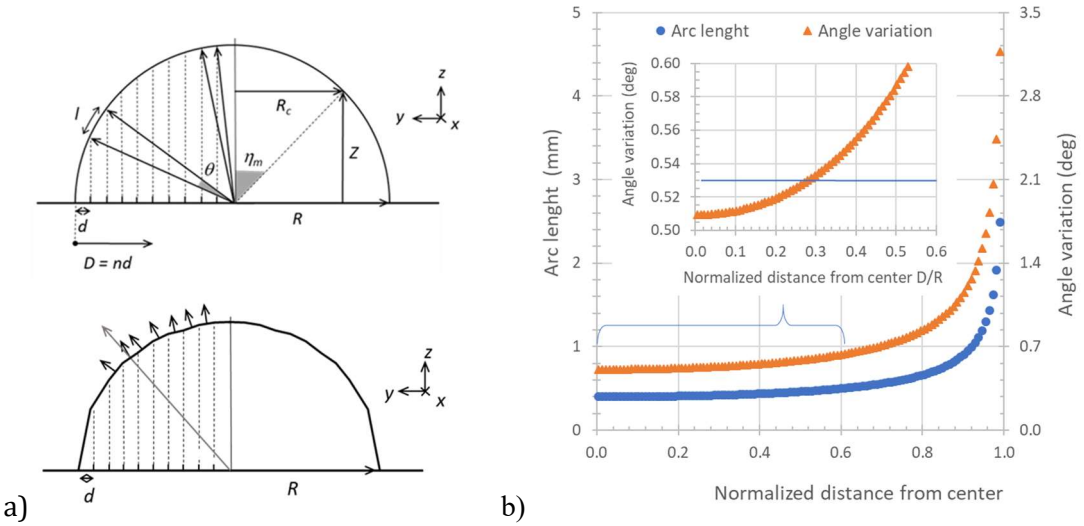

Fig. 4. a) 2D scheme of the effect of planar scan on the cell size and normal angle deviation between neighbouring points/cells. b) Cell size (arc length) and normal angle variations calculated with eqs. (6, 7) and plotted as a function of the distance from the centre of the half-sphere.

The effect of the PB and NA smoothing algorithms on the motion of the printhead TCP along the 3D trajectory was evaluated by varying the number of loops (i.e from 0 to 40 and 0 to 300 for PB and NA, respectively) and retrieving from the robot controller the effective TCP speed and orientation with a sampling period of 4 ms.

3D circuits printing. After the optimization of the printing trajectories, a commercial silver ink (Henkel, Loctite Edag 418SS) was used to print the 3D circuits whose geometry, before and after dying in an air circulation oven (30 min at 90 °C), was recorded with high definition 3D scans (0.05 mm sampling period). Dry circuits were also characterized with an USB optical microscope (Dino-Lite).

Printed circuits geometry (i.e. length and interline pitch) and line section were compared with the theoretical ones, i.e.: the pristine 2D circuit geometry and the line sectional area (A) and height (h) calculated as

$$A = \frac{V_d}{L} \tag{8}$$

and

$$h = \frac{4 \cdot A}{\pi \cdot w} \tag{9}$$

where V_d can be either the wet ink volume

$$V_w = V_0 \cdot n_d \tag{10}$$

or the dry ink volume

$$V_d = V_0 \cdot n_d \cdot \frac{\rho_l}{\rho_d} \quad (11),$$

w is the line width and n_d is the number of drops deposed for a line length L, V_0 is the drop unit volume (i.e. 11.5 10^{-3} mm^3 in the tested jetting conditions), ρ_l and ρ_d are the liquid- and the dry-ink densities, i.e. 1.98 and 3.73 g/cm^3, respectively.

The electric resistance of printed lines was measures using a digital multimeter (Fluke 113) and it was compared to the corresponding theoretical value calculated using the Ohm law and equations 4, 8, 11

$$R = \Omega \, \mathrm{L} \, \frac{V_T}{F_J \, V_d} \quad (12)$$

where Ω is the nominal resistivity of the Ag ink used in this study (i.e. ≤ 7.5 10^{-7} Ohm m), L is the line length (i.e. 35 mm), V_T is the average TCP speed and F_J is the jetting frequency and V_d is the dry ink volume calculated with equation (11).

The shape fidelity and electric resistance of 3D printed circuits and the computational load and processing time were used to evaluate the overall reliability of the developed process.

2.3 3D printed circuit board.

A NFC card reader composed by a hybrid circuit board including a USB PCB, surface mount discrete (SMD) components (resistors, capacitors, transistors, leds), printed interconnections and a NFC antenna, was designed using a commercial PCB designer software (Altium Designer), Fig. 5a. The 3D substrate was constituted by a structural part of the card reader (Fig. 5b) and included a flat region for the USB PCB mount and a connection and a large area concave regions with10 and 90 mm bending radius, respectively.

Optimized printing conditions and geometrical constrains imposed by the 6-axis robot were used to re-design and print the 3D circuit. SMD components were manually placed on the 3D circuit before ink curing (30 min at 90 °C). Line resistance and components characteristics were measured on the final 3D printed board.

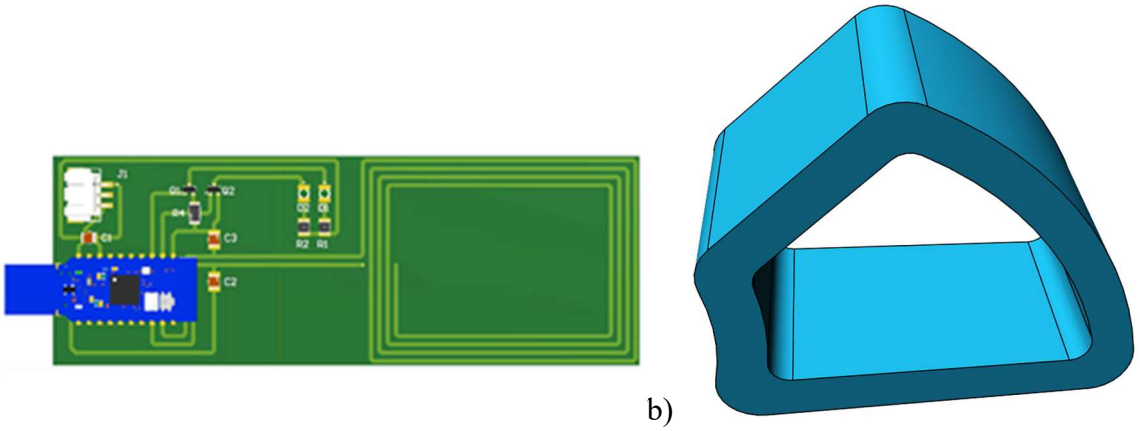

a) b)

Fig. 5. a) 2D design of the NFC reader hybrid PCB including SMD components and b) 3D structural element of the card reader used as printing substrate.

3. Results and discussion

3.1 Effect of PB and NA algorithms on normals alignment.

Noise generated by the laser profilometer during height measurement induced slight deviations in the overall shape of the reconstructed dome. However, the impact on the orientation of mesh cells was not negligible and, as shown in Fig. 6, the average angle variation between neighbouring cells attained 1.8 deg with peaks of 4-5 deg instead of the theoretical 0.53 deg. With the print configuration used in this study (i.e. piezo jetting with a printhead aligned to the normal of the substrate and vertical distance of 2 mm) these uneven angle variations can induce offsets up to 0.16 mm in the target ink deposition point and irregular movements of the 6-axis robot.

Fig. 6 shows that PB smoothing of the pristine mesh efficiently removes the noise and after 20 loops attains the minimum theoretical average angle variation that can be obtained on a 90 mm diameter dome and 0.4 mm sampling period with a minimum dispersion.

Similarly, the application of the NA algorithm to the normals of points lying on the 3D trajectory produced a drop in the average angle which reached the theoretical value of 0.25 deg and minimum dispersion after 20-30 loops (Fig. 7). In the conditions tested in this study, the NA algorithm quickly converged and had a limited computational load compared to PB mesh smoothing (Fig. 8.a).

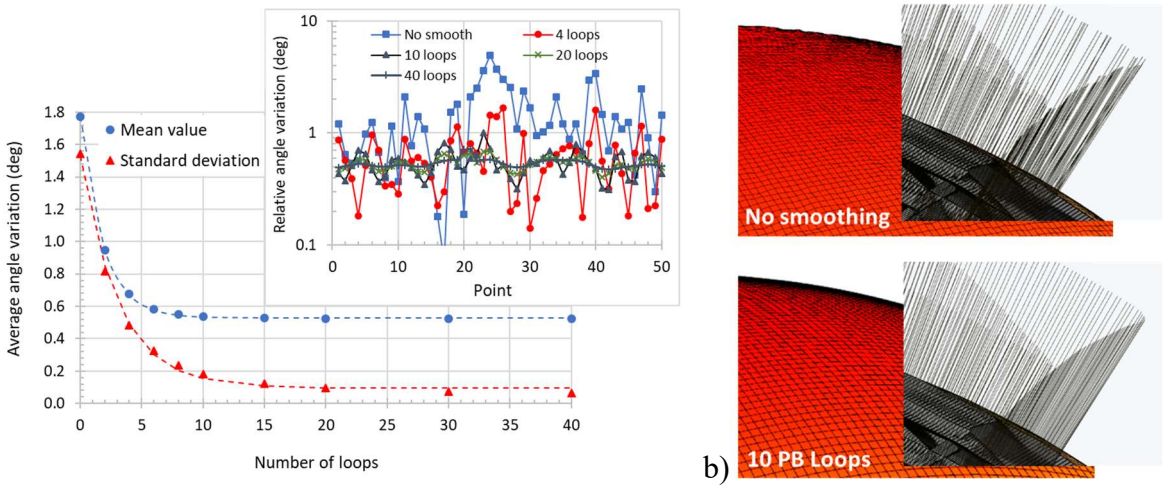

Fig. 6. a) Average normal angle variation and standard deviation along the printing trajectory plotted as a function of the number of loops of the PB smoothing algorithm. Inset shows raw angle variation data. b) Images of the meshed surface and normals before and after 10 loops smoothing.

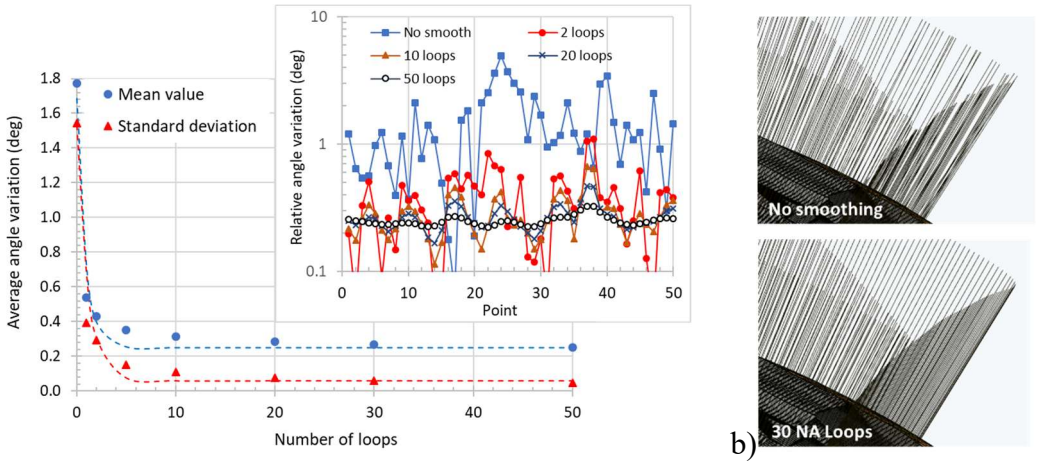

Fig. 7. a) Average normal angle variation and standard deviation along the printing trajectory plotted as a function of the number of loops of the NA smoothing algorithm. Inset shows raw angle variation data. b) Images of the meshed surface and normals before and after 30 loops smoothing.

Owing to the heavy computational load for the relatively small mesh, the large sampling period used in this study (i.e. 3800 mm^2 and 0.4 mm) and the constrain to limit the offset of sampled points position below 0.2 mm, the PB smoothing algorithm was limited to 10 loops. In these conditions the average angle variation was close to the theoretical limit, however individual angles had quite scattered values with standard deviation of 0.2 deg and maximal amplitude of 0.8 deg (Fig. 6.a). The NA algorithm was then used to attain the minimal angle variation of 0.25 deg applying 30 smoothing loops.

Fig. 8.b shows that mesh processing with 10 loops PB smoothing, further increases the convergence of the NA algorithm which attains stable angle variations and standard deviation

values after 3-4 loops corresponding to 72000 operations (i.e. 100 times lower than the computational load required by 10 loops of the PB algorithm). 10 PB loops and 30 NA loops were therefore identified as the best smoothing conditions in order to attain the theoretical angle variation with a minimum computational load.

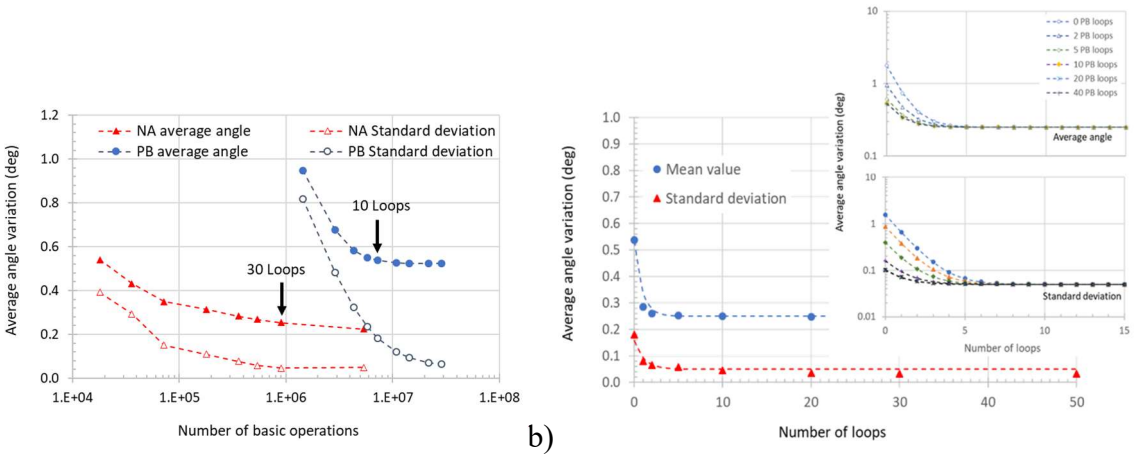

Fig. 8. a) Computational load of the PB and NA smoothing algorithms needed to attain the theoretical angle variation in the tested conditions (i.e. a 50 mm base diameter spherical dome, a 400 mm length circuit and scan and curve discretization periods of 0.4 and 0.2 mm). Arrows indicate when the average angle is close to the theoretical angle variation that can be reached with the PB and NA algorithms, i.e. 0.51 and 0.25 deg, respectively. b) Effect of the NA loops on the convergence of the average angle variation on a mesh already processed with 10 PB loops. Insets show the effect of PB smoothing on the convergence of the NA algorithm.

3.2 Effect of smoothing and circuit design on TCP speed.

TCP speeds retrieved during a blank run along the circuit shown in Fig. 3.a projected on the ABS dome (Fig. 9) show that the sampling noise of the bare mesh affects the TCP trajectory and robot motion which appear discontinuous with abrupt changes in the printhead orientation both along straight lines and right angles. Robot joints are subjected to continuous acceleration/deceleration and, as shown in Fig. 9, the ensuing TCP speed fluctuates between 4 and 14 m/s, well below the targeted 15 mm/s. Filleting right angles with 1 mm radius does not improve TCP speed and oscillations, however a radical improvement in robot motion was obtained applying the optimized PB and NA smoothing conditions. Fig. 9 shows that with a minimum fillet radius of 1 mm the average TCP speed was close to 15 mm/s with minimal fluctuations between 15.7 and 14 mm/s.

The progressive increase of the nominal TCP speed slightly affected the translation speed up to 30 mm/s (Fig. 10.a), when abrupt speed variations start to appear in 4 mm filleted right angles indicating that robot joints are no longer able to provide the angular acceleration needed to

prevent TCP deceleration. Fig. 10.a shows that the further increase of the nominal speed to 50 mm/s led to large fluctuations in the TCP speed. The printhead attains the nominal speed in short segments along the circuit trajectory and most of the time is in a transient acceleration/deceleration regime since in 1 mm filleted right angles the TCP speed drops to ca. 23 mm/s.

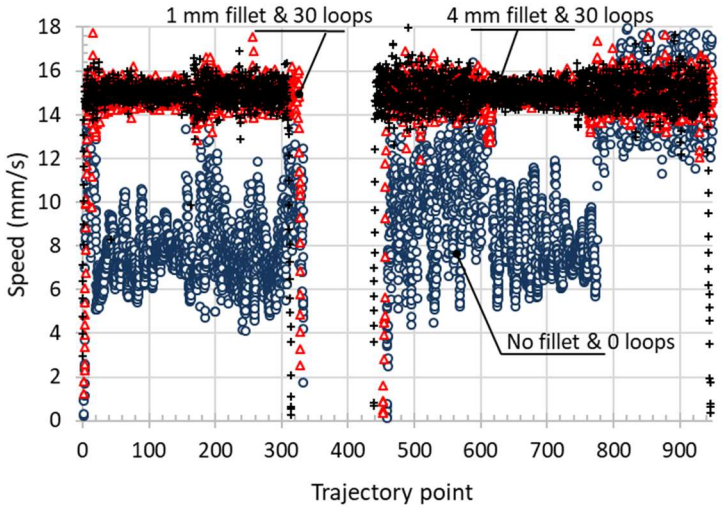

Fig. 9. Effect of normal smoothing and angle fillet on the speed variation of the printhead TCP along the large interdigitated circuit (Fig. 3.a) projected on a 3D mesh smoothed with 10 PB loops. The robot nominal printing speed is 15 mm/s.

Fig. 10.b shows that, despite a slight increase in speed scattering (i.e. the standard deviation), the average TCP speed matches with the nominal speed up to 30 mm/s. Above 30 mm/s the average speed starts to diverge with a pronounced increase of speed fluctuations from 10 to 70% when the nominal speed increases from 15 to 50 mm/s, respectively. According to equation (12) and the proportional correlation between the printing speed and line resistance, a maximum speed fluctuation of ca. 10% was used as constraint to limit line resistance variations in the printed circuit. In the present study, nominal speeds up to 30 mm/s can be used to print linear segments, whereas, in the presence of 1 mm filleted right angles or U turns, the nominal speed should not exceed 15 mm/s.

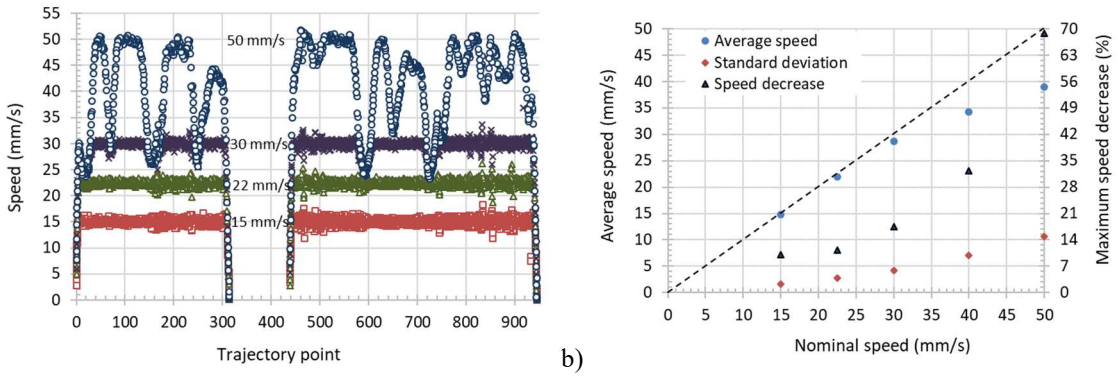

a) b)

Fig. 10. a) Effect of the nominal printing speed on the effective TCP speed along a trajectory with 4 mm filleted angles and processed with 10 PB and 30 NA loops. b) Plot of the average TCP speed along the circuit trajectory and of the maximum speed decrease as a function of the nominal printing speed.

3.3 Geometry and shape fidelity of printed circuits

Fig. 11 shows that circuits printed using the optimized protocol (ie. mesh smoothing with10 PB loops, 2D circuits projection on the 3D mesh, discretization with 0.2 mm segments and normals alignment with 30 NA loops) displayed excellent shape fidelity with no detectable fluctuations in the geometry of printed patterns and a maximum deviation of 2.5% in the length of 3D printed circuits with respect to pristine 2D circuits. 3D scans of the circuit just after ink deposition (Fig. 11.b and 12) showed that printed lines had a 0.265 x 0.20 mm height semi-elliptical section with relatively small variations in width and height. A 10-15% increase in line width was measured in filleted right angles and reflected the local speed decrease from ca. 15 to 13.5 mm/s, as recorded during blank runs. As summarized in Table 1, ink drying led to a decrease of the line height from 0.20 to 0.11 mm. Line width did not change and the resistance of printed lines on a control length of 35 mm was consistent with values calculated with equations (11) and (12), i.e. 0.8 and 0.76 Ohm, respectively. Line width and pitch determined by optical microscopy were ca.10% smaller than those determined using the laser profilometer (i.e 0.46 and 2 mm against 0.53 and 2.1 mm), however this discrepancy was associated with the profilometer sampling period of 0.05 mm and in line with the measurement accuracy and the slight geometrical deformation on ca. 2.5% generated by the planar circuit projection on the half sphere.

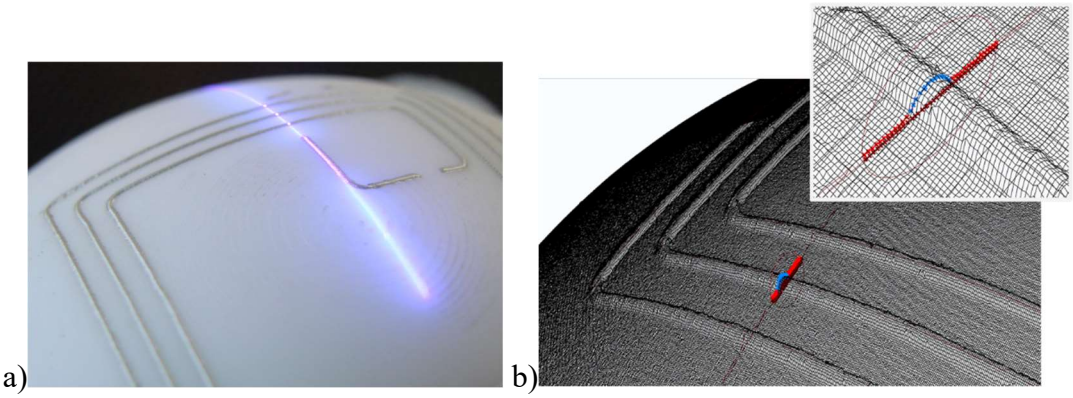

Fig. 11. a) Image of the antenna-type circuit printed on the ABS semi sphere (nominal speed 15 mm/s, jetting frequency 88 Hz). b) Screenshot of the high definition scan used to characterize the circuit geometry after printing (scan sampling period 0.05 mm).

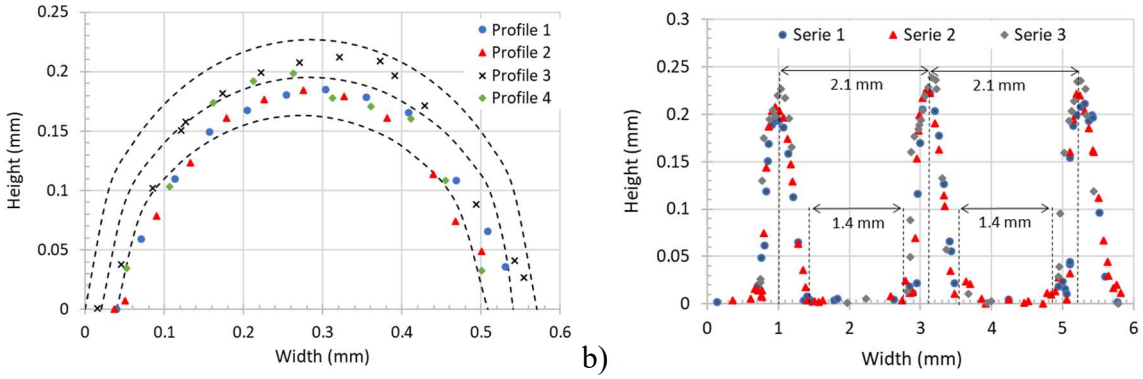

Fig. 12. Section of a) individual printed lines and of b) three lines of the coil before ink drying.

Table 1. Characteristics of circuits shown in Fig. 3a and 3b printed using a nominal speed of 15 mm/s and a jetting frequency of 88 Hz. *The index *w* refers to the wet ink and *d* to the dry ink.

	Straight line			Curve			Coil
	Width (mm)	Height* mm)	Resistance (Ohm)	Width (mm)	Height* (mm)	Resistance (Ohm)	Pitch (mm)
Theoretical	0.44	$0.20_w/0.11_d$	≤ 0.76	0.46	$0.22_w/0.12_d$	≤ 0.64	2
Measured	0.46±0.05	//	0.80±0.05	0.51±0.03	//	//	2±0.03
Measured	0.53±0.05	0.20_w±0.02	//	0.61±0.05	0.21_w±0.02	//	2.1±0.05
from 3D scan		0.12_d±0.03			0.13_d±0.02		

Complex patterns (Fig. 3.c) printed on the ABS dome (Fig. 13.a-e) at a nominal speed of 15 mm/s and a jetting frequency of 75 Hz showed good print quality. Lines width, pitch and electric resistance summarized in Table 2 had values in line with the target tolerance of 10%. Moreover,

1 mm lines gaps (Fig. 13.d) had effective values of 0.70 mm, which was consistent with an expected gap decrease of ca. 0.40 mm induced by the size of individual drops (i.e. 0.40 mm). U turns and zig-zags with bending radius of 0.5 mm (i.e. below the value of 1 mm to limit speed fluctuations to 10%), shown in the encircled patterns in Fig. 13.b, led to a local drop of the effective printing speed from 15 to ca. 10 mm/s (Fig. 13.f) with a subsequent increase of the drop coverage ratio, ink accumulation and a mismatch between the effective printing and jetting time.

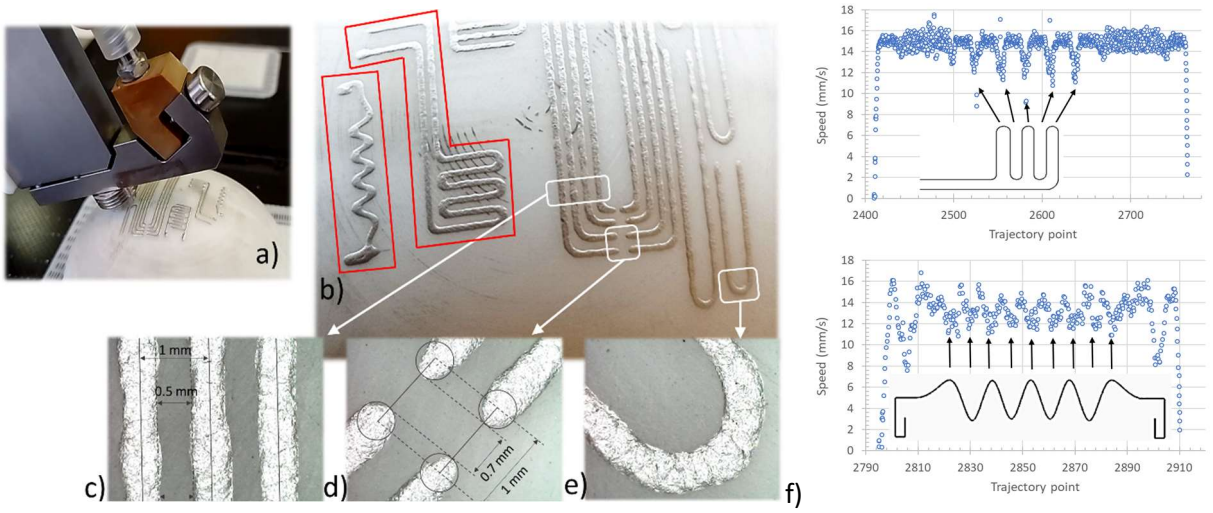

Fig. 13. Patterns with 1 mm pitch shown in Fig. 3.c printed on the ABS dome a), b). Parallel lines with 1 mm pitch and, highlighted in red, forms with bending radius of 0.5 mm c). axial lines with 1 mm gap d) and U turn with 1 mm radius e). Speed fluctuations in forms with bending radius of 0.5 mm, f).

Table 2. Characteristics of the circuit shown in Fig. 3c printed using a nominal speed of 15 mm/s and a jetting frequency of 75 Hz. *The index *w* refers to the wet ink and *d* to the dry ink.

	Straight line			Curve (1 mm radius)			Line
	Width (mm)	Height* mm)	Resistance (Ohm)	Width (mm)	Height* (mm)	Resistance (Ohm)	Pitch (mm)
Theoretical	0.42	$0.18_w/0.10_d$	< 0.90	0.44	$0.2_w/0.11_d$	< 0.76	1
Measured	0.50±0.05	//	0.85±0.05	0.54±0.03	//	//	1±0.02
Measured from 3D scan	0.54±0.05	0.17_w±0.03 0.08_d±0.02		0.58±0.05	0.21_w±0.03 0.10_d±0.02		

Despite the good match between the 2D circuit and the printed one, printed lines displayed periodical width fluctuations when compared to lines printed on a smooth PET films under similar conditions (Fig. 14.a). Those shape defects were ascribed to the typical paths generated during the FDM 3D printing process which, despite an intensive surface polishing, were not removed from the ABS dome thus inducing a deformation of the ink/substrate contact line and

the formation of kinks (Fig. 14.b). Despite the good control of the line pitch during the printing process, line width fluctuations can attain amplitudes of 0.1 mm thus inducing significant variations in the interline distance which, in the tested conditions, ranged from 0.50 to 0.35 mm indicating that a decrease of line pitch to ca. 0.70 mm can lead to lines contact.

Despite the high precision in printhead positioning obtained with the process developed in this study, the surface morphology of the 3D printed substrate represents a major limitation to attain a high print quality and line density. Substrate surface treatment by polishing, sand blasting or by the application of a primer varnish/solvent smoothing will be therefore explored in future work to improve the print quality.

3.4 3D printed hybrid circuit board

Fig. 15a-e summarized the protocol used to project the optimized circuit (Fig. 15.b) on the substrate and to generate 3D trajectories which had a maximum length deviation from the pristine 2D circuit of 1.4%.

The 4-turn antenna coil had a cumulative length (including segments to connect with the USB controller) and resistance of 953 mm and 21.1 Ohms, respectively, which were in line with: i) the resistance of 35 mm control line expected for the printing conditions (i.e. 0.77 Ohm/35 mm vs. the 0.8-0.85 Ohms/35 mm given in Tables 1 and 2), ii) the low coil resistance required in NFC antennas to avoid signal attenuation.

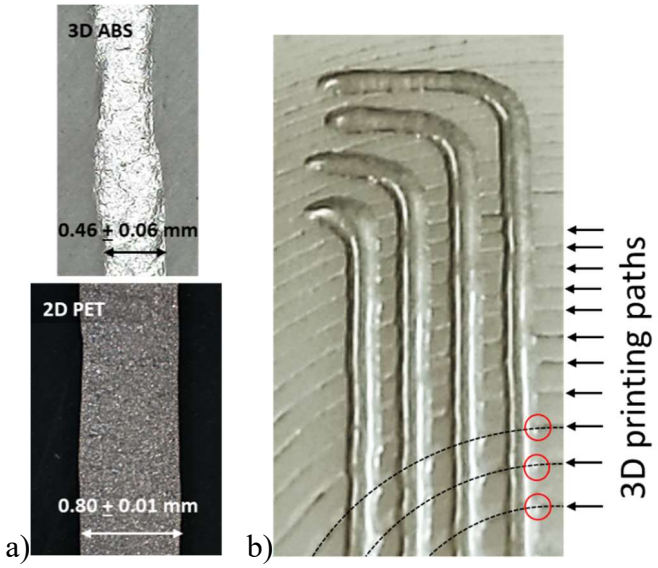

Fig. 14 Comparison of straight lines printed with 60% coverage ratio on smooth PET sheets and on the 3D printed ABS dome a) and image of the periodic line width fluctuations generated by residual 3D printing paths on the polished ABS dome b).

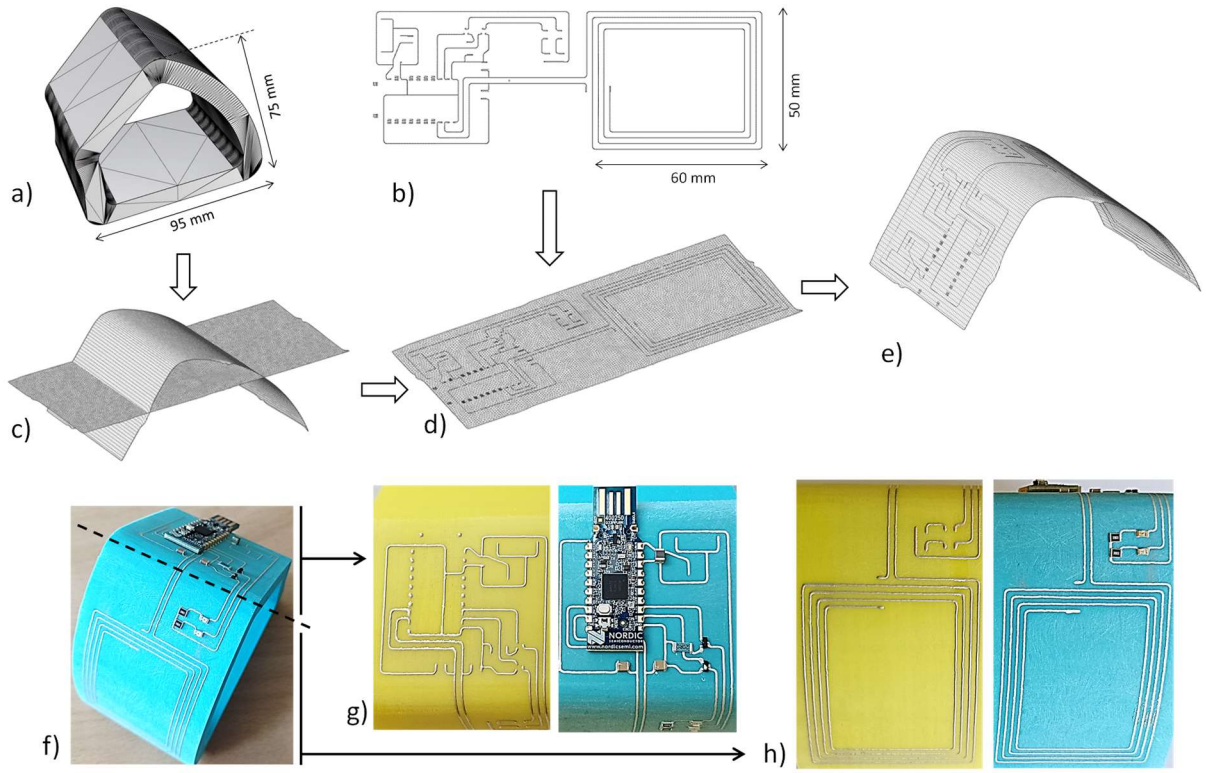

Fig. 15 Design and printing on a 3D substrate of a circuit for badge identification via NFC communication. a) CAD model of the 3D substrate. b) CAD model of the 2D circuit adapted for 6-axis robot printing. c) Scan 3D of the 3D-printed ABS substrate and planarization of the printing region. d) Orthogonal projection of the 2D circuit on the planarized surface. e) Development of the 3D shape and generation of the 3D circuit. f) Final 3D circuit printed on the ABS substrate. g) Detail of the USB controller region before and after components placement. h) Detail of the NFC antenna region before and after components placement.

All SMD components were tested by placing tester electrodes on printed lines at ca. 5 mm distance from component connections. Nominal resistance and capacity values were obtained for 200k-20 Ohms resistors and capacitors, green and red leds worked correctly and neighbouring pins of the USB controller did not display short circuit.

4. Conclusions

Results presented in this work demonstrate that 6 axis industrial robots coupled to high accuracy 3D scan and adequate smoothing algorithms, ie:

- Paul Bourke smoothing of the 3D mesh with an iteration number limited to 10
- Normals alignment of points lying on the trajectory with an iteration number limited to 30

can be effectively used to move a piezo jetting printhead along smooth and high precision trajectories with a nearly constant speed and to print conductive paths on 3D objects.

Moreover, the direct projection of 2D circuits on the planarized mesh and the subsequent 3D development led to a negligible deformation of the pristine 2D circuit (ca. 2% in the tested conditions) and allowed the quick generation of 3D trajectories using standard pre-existing circuit designs.

Trajectories generated on a 3D printed ABS dome and optimized printing conditions (i.e. speed and circuit design) were used to print silver ink circuits which displayed geometry and resistance in line with the semi empirical model developed to predict line width and resistance and the geometry of the pristine 2D circuit. Only the width of printed tracks displayed not negligible wave-like fluctuations which were associated to patterns generated during FDM 3D printing of the ABS dome, thus highlighting the role of substrate surface morphology in affecting the print accuracy.

The optimized circuit design and trajectory processing conditions were successfully used to print a 3D circuit board mimicking a NFC card reader and including a USB PCB, SMD components and a NFC antenna thus showing the viability of the developed process to manufacture low-density 3D PCB.

Overall, this work demonstrates that 6 axis robots coupled to a sequence of unit operations integrated in a control software, i.e.:

i) 3D scan-mesh smoothing,
ii) 2D circuit projection on the planarized mesh and 3D trajectory generation,
iii) normals alignment of points in the 3D trajectory,
iv) retrieve of the effective toolhead TCP translation speed along the 3D trajectory with a blank run,
v) synchronization of the ink jetting frequency with the effective average speed,
vi) generation of the print code and print,

allows to obtain a duty cycle, from the 2D circuit to the 3D printed one, of less than 30 min.

Acknowledgments

This work was supported by the Region Auvergne Rhone Alpes (project R&D Booster 2020 IOT 3D FLEXFAB, grant n° 20 010403 01 – 22437).

References

[1] J. J. Beaman, D. L. Bourell, C. C. Seepersad, D. Kovar, Additive Manufacturing Review: Early Past to Current Practice, J. Manuf. Sci. Eng. 142, 11 (2020) 110812.

[2] U. M. Dilberoglu, B. Gharehpapagh, U. Yaman, M. Dolen, The Role of Additive Manufacturing in the Era of Industry 4.0, Procedia Manufacturing, 11 (2017) 545-554.

[3] P. M. Bhatt, R. K. Malhan, A. V. Shembekar, Y. J. Yoon, S. K. Gupta, Expanding capabilities of additive manufacturing through use of robotics technologies: A survey, Additive Manufacturing 31 (2020) 100933.

[4] P. Urhal, A. Weightman, C. Diver, P. Bartolo, Robot assisted additive manufacturing: A review, Robotics and Computer-Integrated Manuf. 59 (2019) 335-345.

[5] A. Shah, Emerging trends in robotic aided additive manufacturing, Materials Today: Proceedings 62 (2022) 7231–7237.

[6] L. Li, A. Haghighi, Y. Yang, A novel 6-axis hybrid additive-subtractive manufacturing process: Design and case studies, J. Manuf. Proces. 33 (2018) 150–160.

[7] I. M. Nault, G. D. Ferguson, A. T. Nardi, Multi-axis tool path optimization and deposition modeling for cold spray additive manufacturing, Add. Manuf. 38 (2021) 101779.

[8] F. Wulle, O. Gorke, S. Schmidt, M. Nistler, G. E. M. Tovar, O. Riedel, A. Verl, A. Weber, A. Southan, Multi-axis 3D printing of gelatin methacryloyl hydrogels on a non-planar surface obtained from magnetic resonance imaging, Add. Manuf. 50 (2022) 102566.

[9] F. Xie, D. Bi, K.Tang, A potential field based multi-axis printing path generation algorithm, Int. J. Computer Integrated Manuf. 33, 12 (2020) 1277-1299.

[10] A. Hosseini Jafari,N. Gans, Surface parameterization and trajectory generation on regular surfaces with application in robot-guided deposition printing, IEEE Robotics and Autom. Lett. 5, 4 (2020) 6113-6120.

[11] Macdonald, E.; Salas, R.; Espalin, D.; Perez, M.; Aguilera, E.; Muse, D.; Wicker, R. B. 3D Printing for the Rapid Prototyping of Structural Electronics, IEEE Access 2 2014, 2, 234–242. https://doi.org/10.1109/ACCESS.2014.2311810.

[12] Lewis, J. A.; Ahn, B. Y. Device fabrication: Three-dimensional printed electronics. Nature 2015, 518, 42–43. https://doi.org/10.1038/518042a.

[13] B. Lu, H. Lan, H. Liu, Additive manufacturing frontier: 3D printing electronics, Opto-Electronic Advances 1 (2018) 170004.

[14] J. Li, T. Wasley, T. T. Nguyen, V. D. Ta, J. D. Shephard, J. Stringer, P. Smith, E. Esenturk, C. Connaughton, R. Kay, Hybrid additive manufacturing of 3D electronic systems, J. Micromech. Microeng. 26 (2016) 105005.

[15] H. W. Tan, Y. Y. Clarrisa Choong, C. N. Kuo, H. Y. Low, C. K. Chua, 3D printed electronics: Processes, materials and future trends, Progress in Materials Science 127 (2022) 100945.

[16] N. Heininger W. John H.-J. Boßler, Manufacturing of molded interconnect devices from prototyping to mass production with laser direct structuring, In International Congress MID (2004) pp. 1-20. https://www.lpkfusa.com/fileadmin/mediafiles/user_upload/Knowledge_Center/mid_conference_09-2004.pdf

[17] B. Bachy, Experimental Investigation and Optimization for the Effective Parameters in the Laser Direct Structuring Process, J. Laser Micro Nanoeng. 10 (2015) 202–209.

[18] M. Bakr, Y. Su, F. Bossuyt, J. Vanfleteren, Effect of overmolding process on the integrity of electronic circuits, in: 2019 22nd European Microelectronics and Packaging Conference & Exhibition (EMPC), IEEE, Pisa, Italy, 2019: pp. 1–8. https://doi.org/10.23919/EMPC44848.2019.8951797.

[19] A.Huttunen, T. Kurkela, K.-L. Vaisanen, E. Juntunen, Multilayer plastic substrate for electronics, in: 2018 7th Electronic System-Integration Technology Conference (ESTC), IEEE, Dresden, 2018: pp. 1–6. https://doi.org/10.1109/ESTC.2018.8546335

[20] Ledesma-Fernandez, J.; Tuck, C.; Hague, R. High viscosity jetting of conductive and dielectric pastes for printed electronics. Proceed. of the Int. Solid Freeform Fab. Symp. 2015, 40-55.

[21] Seifert, T.; Sowade, E.; Roscher, F.; Wiemer, M.; Gessner, T.; Baumann, R. R. Additive manufacturing technologies compared: morphology of deposits of silver ink using inkjet and aerosol jet printing. Ind. & Eng. Chem. Res. 2015, 54(2), 769-779.

[22] Tricot, F.; Venet, C.; Beneventi, D.; Curtil, D.; Chaussy, D.; Vuong, T. P.; Broquin, J. E.; Reverdy-Bruas, N. Fabrication of 3D conductive circuits: print quality evaluation of a direct ink writing process. RSC Adv. 2018, 8, 26036–26046. https://doi.org/10.1039/C8RA03380C.

[23] G. Furia, F. Tricot, D. Chaussy, P. Marin, A. Graziano, D. Beneventi, Use of a 6-axis robot and ink piezo-jetting to print conductive paths on 3D objects. Printed circuit geometry, and conductivity predictive model, CIRP J. Manuf. Sci. Tech. 35 (2021) 855-863.

[24] C. Delfaut, T.-P. Vuong, A. Niembro-Martin, T. Lacrevaz, Q.-B. Duong, D. Paulet, D. Curtil, J.-E. Broquin, C. Venet, N. Reverdy-Bruas, Study of feasibility for 2D and 3D innovative jet printed RF devices, 16th European Conference on Antennas and Propagation (EuCAP), Madrid, Spain (2022) pp. 01-04, doi: 10.23919/EuCAP53622.2022.9769262.

[25] T. H. Le Dam, A. Niembro-Martin, T. Lacrevaz, G. Houzet, C. Delfaut, D. Paulet, N. Reverdy-Bruas, Q. Bao Duong, T. Phu Vuong, Study of a 3D FSS-Based Printed Radome Demonstrator for a Patch Antenna at 3.6 GHz," 2022 52nd European Microwave Conference (EuMC), Milan, Italy (2022) pp. 664-667, doi: 10.23919/EuMC54642.2022.9924470.

[26] L. Riviere, J. Munoz, Les enjeux de l'impression directe de fonctions radiofréquence sur pièces 3D, Mecaplastronic Connection 2022, 29-30 novembre 2022, Lyon. https://cdn-assets.inwink.com/af4e599d-f84a-4edf-bec2-f0bbe2e725ea/d7dc9601-b18f-4a1d-9cb4-826e04df5ddb

[27] B. Bao, H. Moeinnia, T.-H. Kim, W. Lee, W. S. Kim, 3D Structural electronics via multi-directional robot 3D printing, Adv. Mater. Technol. 2022, 2201349.

[28] P. Bourke, Surface Relaxation and Smoothing, Geometry, Surfaces, Curves, Polyhedra: Notes on Polygon and Meshes (1997), http://paulbourke.net/geometry/polygonmesh/

[29] S. Sechelmann, T. Rörig, A. I. Bobenko, Quasiisothermic Mesh Layout, Advances in Architectural Geometry, Hesselgren, L.; Sharma, S.; Wallner, J.; Baldassini, N.; Bompas, P.; Raynaud, J. (Eds.). (2012), p. 285. ISBN 978-3-7091-1250-2